Cosmic ray energy reconstruction from the S(500) observable recorded in the KASCADE-Grande air shower experiment

Cosmic ray energy reconstruction from the $S(500)$ observable recorded with the KASCADE-Grande air shower experiment

W.D. Apel[a], J.C. Arteaga-Velázquez[b], K. Bekk[a], M. Bertaina[c], J. Blümer[a,d], H. Bozdog[a], I.M. Brancus[e], E. Cantoni[c,f,1], A. Chiavassa[c], F. Cossavella[d,2], K. Daumiller[a], V. de Souza[g], F. Di Pierro[c], P. Doll[a], R. Engel[a], D. Fuhrmann[h,3], A. Gherghel-Lascu[e], H.J. Gils[a], R. Glasstetter[h], C. Grupen[i], A. Haungs[a,*], D. Heck[a], J.R. Hörandel[j], D. Huber[d], T. Huege[a], K.-H. Kampert[h], D. Kang[d], H.O. Klages[a], K. Link[d], P. Łuczak[k], H.J. Mathes[a], H.J. Mayer[a], J. Milke[a], B. Mitrica[e], C. Morello[f], J. Oehlschläger[a], S. Ostapchenko[l], N. Palmieri[d], M. Petcu[e], T. Pierog[a], H. Rebel[a], M. Roth[a], H. Schieler[a], S. Schoo[a], F.G. Schröder[a], O. Sima[m], G. Toma[e,*], G.C. Trinchero[f], H. Ulrich[a], A. Weindl[a], J. Wochele[a], J. Zabierowski[k]

[a] *Institut für Kernphysik, KIT - Karlsruhe Institute of Technology, Germany*
[b] *Universidad Michoacana de San Nicolas de Hidalgo, Inst. Física y Matemáticas, Morelia, Mexico*
[c] *Dipartimento di Fisica, Università degli Studi di Torino, Italy*
[d] *Institut für Experimentelle Kernphysik, KIT - Karlsruhe Institute of Technology, Germany*
[e] *Horia Hulubei National Institute of Physics and Nuclear Engineering, Bucharest, Romania*
[f] *Osservatorio Astrofisico di Torino, INAF Torino, Italy*
[g] *Universidade São Paulo, Instituto de Fîsica de São Carlos, Brasil*
[h] *Fachbereich Physik, Universität Wuppertal, Germany*
[i] *Department of Physics, Siegen University, Germany*
[j] *Department of Astrophysics, Radboud University Nijmegen, The Netherlands*
[k] *National Centre for Nuclear Research, Department of Astrophysics, Łódź, Poland*
[l] *Frankfurt Institute for Advanced Studies (FIAS), Frankfurt am Main, Germany*
[m] *Department of Physics, University of Bucharest, Bucharest, Romania*

Abstract

The energy reconstruction at KASCADE-Grande is based on a combination of the shower size and the total muon number, both estimated for each individual air-shower event. We present investigations by a second method to reconstruct the primary energy using $S(500)$, the charged particle densities inferred with the KASCADE-Grande detector at 500 m distance from the shower axis. We account for the attenuation of inclined showers by applying the 'Constant Intensity Cut' method and we employ a simulation derived calibration to convert the recorded $S(500)$ into primary energy. We observe a systematic shift of the $S(500)$-derived energy in relation to the earlier published results of the standard reconstruction technique. However, a comparison of the two methods on simulated and measured data shows that this shift appears only for measured data. Investigations show that this shift is mainly caused by the insufficient way simulations describe the shape of the lateral density distribution.

Keywords: cosmic rays, primary energy, KASCADE-Grande, $S(500)$, hadronic interaction models

1. Introduction

Cosmic rays experiments are mainly concerned with inferring the arrival direction, the energy spectrum and the elemental composition of the primary cosmic radiation. The primary energy spectrum falls steeply and extends up to 10^{20} eV. Two features are immediately visible in the spectrum, in the form of two spectral index changes. These features produce a shape of the spectrum similar to a bent human leg hence their names: *knee* (steepening of the spectrum) and *ankle* (flattening). The two features are strongly correlated in the models describing their source (e.g. [1, 2]). It is generally accepted that towards the highest energies ($E_0 > 5 \times 10^{18}$ eV), the component above the ankle is

*Corresponding authors
Email addresses: andreas.haungs@kit.edu (A. Haungs), gabriel.toma@outlook.de (G. Toma)
[1] now at: Istituto Nazionale di Ricerca Metrologia, INRIM, Torino, Italy
[2] now at: DLR Oberpfaffenhofen, Germany
[3] now at: University of Duisburg-Essen, Duisburg, Germany

most likely of extragalactic origin [3]. Towards lower energies (i.e. $E_0 \approx 4 \times 10^{15}$ eV), the knee is caused by a rigidity dependent extinction of the light component in the galactic radiation.

The KASCADE-Grande [4] experiment has been designed to record extensive air showers (EAS) in the 10^{16}-10^{18} eV energy range to answer such questions regarding the transition to the extragalactic radiation. Recent results at KASCADE-Grande [7] show a flux of cosmic rays in very good agreement with results of other experiments (e.g. KASCADE [5], EAS-TOP [6]). The all-particle energy spectrum reported by KASCADE-Grande exhibits a hardening of the spectrum at 2×10^{16} eV, a knee-like feature at around $10^{16.92}$ eV due to heavy primaries and an ankle-like hardening at $10^{17.08}$ eV due to the light component [7, 8, 9]. These results were provided by a reconstruction technique based on a N_{ch}-N_{μ} correlation (i.e. total shower size - muon size) used to infer the primary energy from the data recorded by KASCADE-Grande.

In this paper we present a second approach to reconstruct the primary energy with KASCADE-Grande. This approach is applied independently from the standard method and to the same shower sample leading to subsequent cross-checks between results. The new method is based on a specific primary energy estimator, the attenuation-corrected charged particle density at 500 m distance from the shower axis, $S(500)$. The interest in such observable (i.e. the signal at a fixed radial distance) was particularly justified for a loosely spaced detector array such as AGASA [10] where the total shower size could not be evaluated on an event by event basis (although this is not the case of the KASCADE-Grande experiment).

2. KASCADE-Grande

The KASCADE-Grande [4] detector array was situated at the site of the Karlsruhe Institute of Technology - KIT, Campus North, Germany (49° N, 8° E) at 110 m a.s.l. It had a roughly rectangular shape with a length of 700 m (Fig. 1 *left*) and was a multi-detector system. Several types of detectors enabled the measurement of different EAS observables. The studies in this paper are based on measurements of the lateral distribution of charged particle densities in EAS.

Historically, the KASCADE-Grande detector was an extension of a smaller array, the KASCADE [5], operated since 1996. KASCADE was a complex detector aimed to clarify the origin of the knee in the primary energy spectrum. It was therefore designed to record air showers initiated by primaries with energies in the

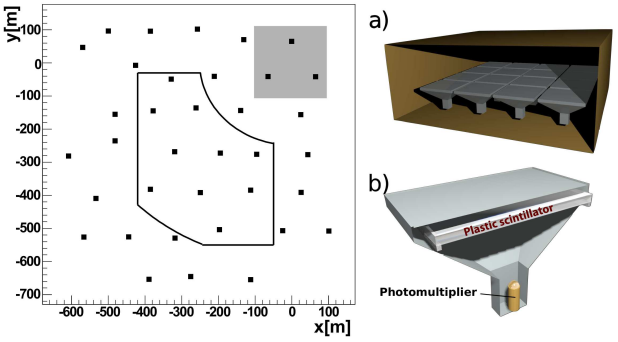

Figure 1: *Left*: schematic top-view of the KASCADE-Grande detector array (the Grande stations are shown as square dots and the fiducial area with line contour, see text) and the area covered by KASCADE (as shaded rectangle); *Right a)* simplified 3D view of the inside of a Grande station; *Right b)* inside view of a scintillator module.

10^{14} - 10^{16} eV range. By design KASCADE could record numerous observables associated with the electromagnetic, muonic and hadronic EAS components.

The decision to extend the KASCADE array was guided by the intention to expand the EAS observations towards primary energies in the 10^{16} – 10^{18} eV range, with focus on the expected transition from galactic to extragalactic cosmic rays. In particular, measurements in this energy range could clarify whether there exists a second knee-like structure in the energy spectrum. Recording higher energy air showers presented specific challenges which guided the extension of KASCADE to KASCADE-Grande. Extensive air showers initiated by higher energy primaries contain more particles and cover a wider area at the observation level. These showers tend to saturate the detectors close to the shower core. At the same time, in order to better describe larger events, it is necessary to sample information from a wider radial range in the lateral particle density distributions. Another aspect is that larger EAS events (produced by higher energy primaries) occur less frequently. The solution was to expand the sensitive area of the existing detector by installing an additional array (the Grande array) with increased spacing between stations and covering a wider area, thus creating the KASCADE-Grande.

The Grande array consisted of 37 detector stations (formerly part of the EAS TOP array [6]), arranged on the ground in a roughly hexagonal grid with a spacing of about 140 m (Fig. 1 *left*). Each station consisted of a metal hut housing 16 plastic scintillation detectors organized in a 4×4 pattern (Fig. 1a). Each scintillator was 80×80 cm wide and 4 cm thick and was enclosed in

a pyramidal steel casing (Fig. 1b). The scintillator was viewed from below by a high gain photo-multiplier. The 4 central modules in each station were equipped also with low gain photomultipliers. The total effective area was 10 m^2 per station.

KASCADE-Grande was in operation from 2003 until 2013, and is meanwhile dismantled.

3. Reconstruction of $S(500)$

3.1. $S(500)$ as energy estimator

Previous investigations have shown that the charged particle density in air showers becomes independent of the primary mass at a large but fixed distance from the shower axis and that it can be used as an estimator for the primary energy [11]. In a comparison between the p and Fe initiated showers, the $e^{+/-}$ excess in p showers towards lower radial ranges diminishes with the increase of the distance to the shower axis as the electrons get absorbed. At the same time the muon excess in the Fe showers gradually becomes more important at larger radial ranges. Following this trend, for a given radial range this behavior produces an overlap of the lateral distributions (Fig. 2) and in that location the value of the charged particle density becomes mass independent. Such a distance is specific for a given experiment as it depends on the observation level and on the detector threshold and sensitivity to the charged particle component. Based on this property a method was derived to reconstruct the primary energy from the particular value of the charged particle density, observed at such specific radial distances. While in the AGASA experiment the technique was applied for a distance of 600 m to the shower axis [10], in the case of the KASCADE-Grande array detailed simulations [12] have shown that the particular distance for which this effect takes place is about 500 m (Fig. 2), hence the notation $S(500)$ for the charged particle density at 500 m distance from the shower axis. The distance is measured in a plane normal to the shower axis and containing the shower core. The property of mass independence is visible also in Fig. 3 showing the correlation between the energy estimator $S(500)$ and the primary energy for different primary masses.

It must be stressed that the properties of the $S(500)$ observable are predicted by simulation studies based on the QGSJet-II-2 [14] hadronic interaction model and it is entirely possible that simulations based on other interaction models could predict different mass-independent observables. Tests have shown however that in the case of KASCADE-Grande the S(500) remains usable [17] with other models such as EPOS 1.99 [18], QGSJet-II-4 [19] and EPOS-LHC [20].

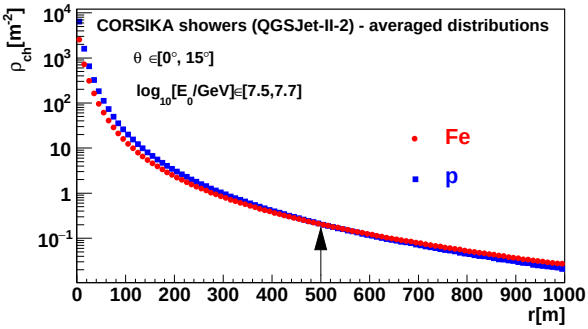

Figure 2: Averaged simulated lateral distributions for p and Fe primaries with energy in a narrow range.

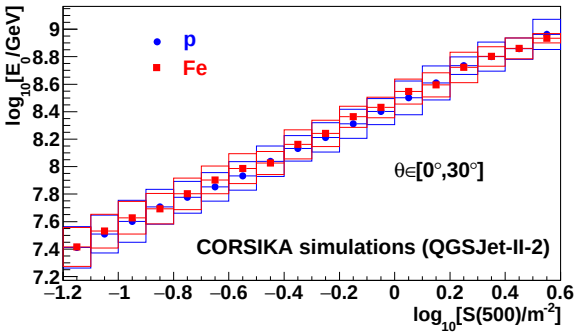

Figure 3: The dependence of the primary energy E_0 on the $S(500)$ for p and Fe primaries (simulated showers in fairly equal proportions for the two masses); the boxes show the spread of data, the errors on the mean are dot-sized.

3.2. Event selection

Simulated showers are used for fine tuning the reconstruction procedure and also for calibrating the observable of interest, $S(500)$ with the primary energy. The analysis is applied identically to simulated and experimental events using the same reconstruction procedure.

Air showers are simulated using the CORSIKA [13] Monte Carlo EAS simulation tool, with the QGSJet-II-2 [14] and FLUKA [15, 16] models embedded. A thinning procedure is not applied. The set of simulated showers includes events simulated for 5 primaries (p, He, C, Si and Fe in fairly equal proportions) with continuous energy spectrum between $10^{15} - 3\times10^{18}$ eV and with a spectral index $\gamma = -2$ harder than the measured data. The harder spectral index allows to faster increase the statistical accuracy at higher energies by not simulating as many showers at lower energies as in a $\gamma \approx -3$

sample. Since the spectral index of simulations is significantly different from the experimentally observed one, a weighting is applied to simulated events in most of the subsequent studies to emulate a softer energy spectrum $\gamma = -3$. About 3×10^5 events have been simulated for each primary. The arrival direction of showers is isotropical and the shower cores are spread randomly on an area larger than the Grande array. In addition, for comparisons smaller sets of showers have been simulated using the high energy hadronic interaction models EPOS 1.99, QGSJet-II-4 and EPOS-LHC.

To select a high quality shower sample a set of quality cuts is applied identically to the simulated events and to the data. The fiducial area (as shown in Fig. 1) has been chosen to be the same as in [7] in order to increase the similarity of selected shower samples in both reconstruction approaches. The fiducial area is a rectangle omitting the closest and farthest corners relative to the KASCADE array in order to minimize the under- and overestimation on the muon number which is relevant for the standard reconstruction approach [7]. For the present studies at least 25 triggered stations are required in every event. For a station to be valid it must provide trigger time information and be correlated with the event within in a given time window. Another quality cut is concerned with the zenith angle of incidence which is limited to only up to 30°. This condition is intended to minimize geometrical effects due to shower inclinations and to reduce the fraction of showers that have no information in the lateral density distribution at large radial ranges. Following these quality cuts and taking into account the chosen fiducial area, on average there are 28 triggered stations in each event. About half of all events have recorded data at 500 m. Most triggered stations are therefore below 500 m distance from the shower axis. The acceptance of the experiment under the above mentioned assumption for fiducial area and zenith angle is 1.28×10^5 m^{2}sr. The total acquisition time is 1503 days leading to an exposure of $1.66{\times}10^{13}$ m^{2}s sr.

3.3. The reconstruction of $S(500)$

The reconstruction procedure that is described in the following is applied without any change to both simulated and experimental events [21].

The KASCADE-Grande detector stations record the energy deposits of particles and the associated temporal information (arrival times of particles) without disentangling the particle type (e.g. muons from electrons). The temporal information is used to reconstruct the zenith and azimuth angles of the shower axis [22]. The recorded energy deposit is converted to particle densities using appropriate Lateral Energy Correction Functions (LECF) [23] that take into account the arrival direction of the shower and the azimuthal position of each station around the shower axis.

For both experimental and simulated events, the information of energy deposit is usually given in the detector plane. Particle densities are reconstructed however in the plane normal to the shower axis [24] as shower properties are better revealed in this plane. In order project the shower information from the detector plane onto the normal plane, special care was taken in order to avoid distorting it. For an inclined shower, the particle density around the shower core at a given radial range can vary due to different particle absorption and scattering in the atmosphere. A relevant example is the case of particles in the lower half of the EAS particle front, as opposed to those in the upper half for an inclined shower. The particles in the lower part of the EAS front will travel a shorter distance through atmosphere before reaching the detector level. If detectors are placed predominantly under the shower axis, the particle density would be overestimated (following that in the opposite case the density would be underestimated). Furthermore, the angle of incidence of particles in detectors will be different in the two cases because the particles have a transverse momentum and do not propagate parallel to each other or to the shower axis. The error in the density influences both the reconstructed shower size and the accuracy of shower core reconstruction. A procedure has therefore been introduced in order to compensate for the attenuation of inclined showers. In addition the dependence of energy deposits with the angle of incidence of particles is also taken into account.

To calculate the charged particle density at 500 m distance from the shower axis, the lateral density distribution is approximated with a 3-parameter Linsley function (eq. 1,2)[25] (we exclude from the analysis the information within a small radial range around the shower core to avoid effects introduced by saturated stations) [4]:

$$\rho_{ch} = \frac{N}{r_0^2} \cdot C(\alpha, \eta) \cdot \left(\frac{r}{r_0}\right)^{-\alpha} \cdot \left(1 + \frac{r}{r_0}\right)^{-(\eta-\alpha)} \quad (1)$$

where

$$C(\alpha, \eta) = \Gamma(\eta - \alpha) \cdot \left[2\pi \cdot \Gamma(2 - \alpha) \cdot \Gamma(\eta - 2)\right]^{-1} \quad (2)$$

[4] For applying an independent analysis also a different LDF-function was chosen compared to the standard approach. However, investigations have shown that both functions work equally well in determining $S(500)$ (for both simulated and experimental events).

with
ρ_{ch} (r) - charged particle density at distance r[m] from the shower core;
N - shower size (in this case the total number of charged particles);
r_0 - Molière type radius [m];
r - radius [m];
α, η - two shape parameters.
The shower core is reconstructed iteratively. In a first approximation it is obtained as the center of mass of the energy deposits in stations. This result is afterwards refined using a Linsley fit of the lateral distribution in which the α and η parameters are fixed. A similar iterative method is used in the standard reconstruction at KASCADE-Grande. The shower core reconstruction is applied identically for data and simulated events.

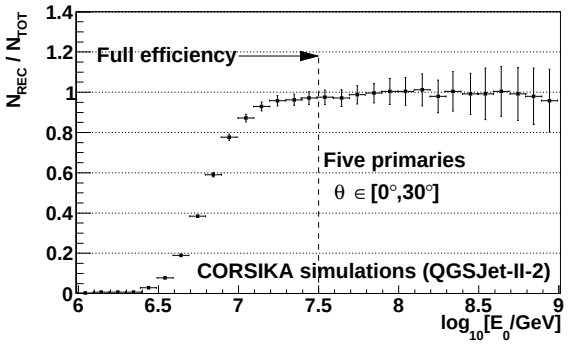

Figure 4: Ratio between the number of simulated events for which $S(500)$ was successfully reconstructed and the total number of simulated events as a function of the primary energy (the energies of the simulated events are distributed as a power law with spectral index γ=-2).

Fig. 4 shows that the fraction of successfully reconstructed $S(500)$ in simulated events exceeds 95% at around $\log_{10}(E_0/\mathrm{GeV}) = 7.5$. The fluctuations around the value 1 for energies $\log_{10}(E_0/\mathrm{GeV}) > 7.5$ are due to the fluctuation of reconstructed shower cores inside or outside the fiducial area that is used for shower selection. Approximately 9.05×10^5 experimental events have passed all imposed selection cuts and had the S(500) successfully reconstructed. In contrast to the $S(500)$-based method, the full efficiency of the standard reconstruction procedure [7] (based on N_{ch} - N_μ) is reached at lower energies, $E_0 \approx 10^{16}$ eV. This is mainly due to the shower selection procedure (Section 3.2) that is employed to maximize the reconstruction quality of $S(500)$, at the expense of slightly reduced efficiency.

The recorded $S(500)$ values can not be directly converted to primary energy without first accounting for the different attenuation of inclined events in the atmosphere. This is achieved by applying the Constant Intensity Cut (CIC) method that corrects all recorded $S(500)$ values as if the showers were coming from a fixed zenith angle (Appendix A). The zenith angular distribution in the 0°-30° peaks at ≈ 21°, hence this value was chosen as CIC reference angle. The measured S(500) spectrum is shown in Fig. 5.

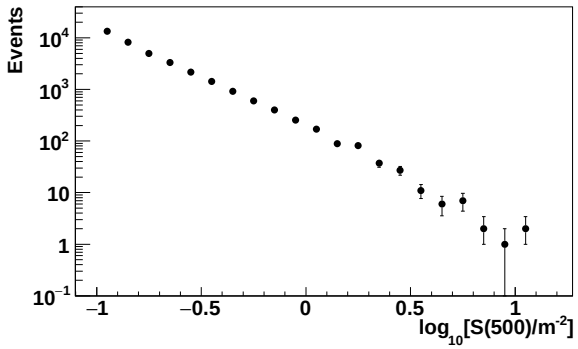

Figure 5: The measured S(500) spectrum after the CIC correction.

4. Energy reconstruction

4.1. Energy reconstruction using $S(500)$

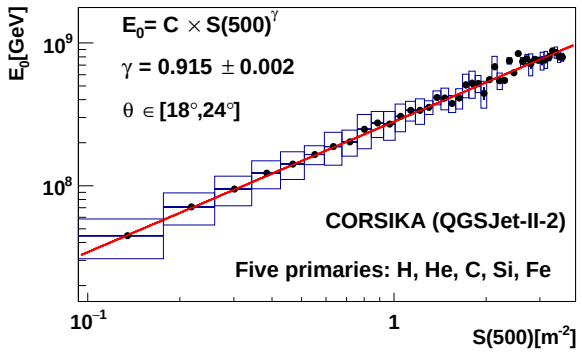

Figure 6: E_0 - $S(500)$ correlation; the dots are the profile of the scatter plot with box errors showing the spread of data while errors of the mean are dot sized; the continuous line is a power law fit with γ=0.915±0.002.

A calibration is derived from simulated showers with zenith angle around the CIC reference angle and with a mass composition of 5 primaries in fairly equal proportions. Fig. 6 shows the calibration using CORSIKA simulations with QGSJet-II-2. Calibrations obtained for the other interaction models are very similar and not shown. The calibration is a power law function as in

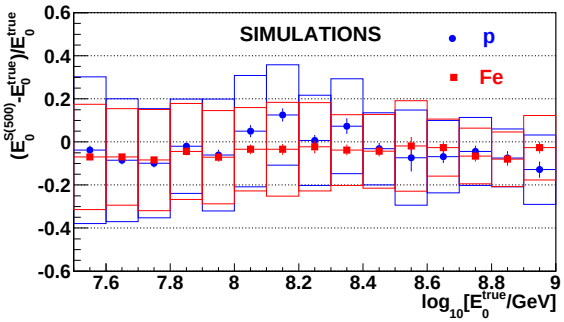

Figure 7: Energy resolution - the box errors show the spread of data while the error of the mean with bar is dot sized; the plot shows the case of p and Fe primaries and a similar behavior is noted for other primaries too.

eq. 3 and is used to convert all attenuation-corrected $S(500)$ values to the corresponding primary energy.

$$E_0 = C \cdot S(500)^{\gamma} \quad (3)$$

with C - a constant; and γ - the slope index of the power law dependency.

Under the assumptions of the QGSJet-II-2 model the energy calibration is found to be composition independent. In order to test the method ability to reproduce the primary energy values we calculate the energy resolution. For the simulated shower sample we show the relative difference between the reconstructed primary energy and the true energy as a function of the primary energy (Fig. 7). The RMS of the distribution (i.e. energy resolution) has an overall value of 25% and it improves slightly with the increase of energy. This is due to the decrease of shower to shower statistical fluctuations at higher energies. Fig. 7 shows also that there is a slight ($\approx$ 5%) underestimation of the primary energy, more so towards lower energies, but still below 10%. This appears in the case of small showers where the lateral particle density has little or no data towards r = 500 m causing the Linsley fit to better describe the range closer to the shower core which is much steeper hence leading to an underestimation of the density value at 500 m.

4.2. Comparison between results

In order to ensure that the method based on $S(500)$ is working correctly we evaluate the energy reconstruction by this and the standard method [7] on an event-by-event basis first for simulations and then for data.

Figure 8 shows the comparison between the reconstructed energy spectra in the two methods and the true energy for the same shower sample (in this plot we represent the result of each method relative to the true energy distribution that is used in simulations). We conclude that for simulated showers both reconstruction methods function similarly as the results of each one agrees reasonably well with the other. At the highest energy it was found that less events could be reconstructed with the true energy due to low statistics in the simulated sample.

In the following a similar test is performed for ex-

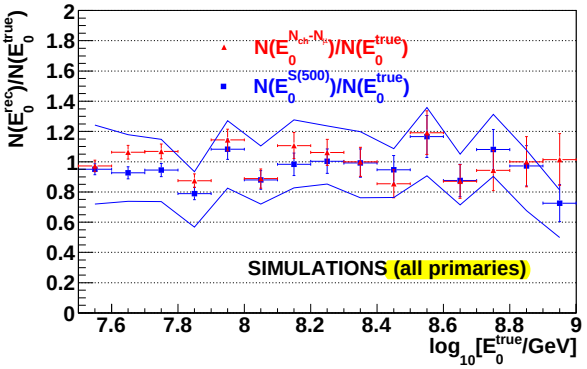

Figure 8: Bin by bin ratio between the reconstructed energy distribution (number of events in each energy bin) and the true energy distribution when reconstructing CORSIKA simulated showers in the two approaches; the continuous lines show the estimated systematic uncertainty for the $S(500)$-derived distribution (see Appendix C).

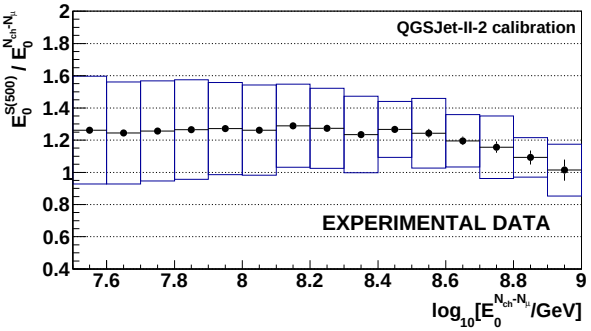

Figure 9: Ratio between the energy from $S(500)$, $E_0^{S(500)}$ and the reconstructed energy in the standard approach, $E_0^{N_{ch},N_\mu}$; the plot is a profile with box errors showing the spread of data and the bar errors the error of the mean.

perimentally recorded data. In Fig. 9 we plot the ratio between the reconstructed primary energy from the described approach ($E_0^{S(500)}$) and from the standard reconstruction ($E_0^{N_{ch}-N_\mu}$), for an experimental shower sample that has been reconstructed by both methods. We note that unlike the case of simulations (Fig. 8), for data

$E_0^{S(500)}$ has systematically higher values (up to 30%) than $E_0^{N_{ch}-N_\mu}$. The difference is not constant over the entire accessible energy range and seems to diminish at the highest energies above $\log_{10}[E_0^{N_{ch}-N_\mu}/\mathrm{GeV}] \approx 8.4$. This is likely due to the variation with energy of the ratio between the electron and muon sizes, not reflected in the S(500) value.

Applying a correction to the estimated resolution by a response matrix (unfolding), the energy spectrum based on the $S(500)$ observable could be determined. But, as we observe a systematic shift in the estimated energy compared to the standard method applied to the KASCADE-Grande detected events, we focus on the investigation of the source of this shift. The unfolding procedure, the determination of the spectrum, as well as the discussion of the uncertainties are described in Appendix B and Appendix C.

4.3. Discussion

Considering that we are using the same procedure for the reconstruction of both simulated and experimental data, the disagreement between the two reconstructions in data (although they were in good agreement in the simulation) might indicate that certain features of the EAS are not described accurately by simulations. Such features are the shape of the lateral distribution, the shower size, the position of the shower maximum or the attenuation of the particle number in the atmosphere. As a test we compare the shower size (N_{ch}) for p and Fe simulations and for the experimental data, when selecting showers in the same narrow energy range (selected by same $S(500)$). For showers detected by KASCADE-Grande in the $10^{16} - 10^{18}$ eV energy range we expect that for a given $S(500)$ (i.e. fixed energy) the observed N_{ch} will be in a range delimited by p and Fe assumptions [1, 2]. We use the value of N_{ch} as inferred on an event by event basis from a modified NKG fit [27] of the lateral distribution as in the standard approach [7] (Fig. 10). For various $S(500)$ ranges in Fig. 10 we observe that the data do not satisfy the expectations and indicates a mass composition heavier than Fe. This is in agreement with Fig. 11 where we compare averaged lateral density distributions for simulated showers (p and Fe primaries) and data. The experimental lateral distribution is outside the p and Fe predictions towards elements heavier than Fe.

We evaluate this disagreement in a bit more detail. Based on Fig. 10 we impose a change on an event by event basis on the measured $S(500)$ by decreasing the reconstructed $S(500)$ values with a value of $\Delta[\log_{10}\mathrm{S}(500)/\mathrm{m}^{-2}] = -0.1$. The value -0.1 for this correction is the minimum one must introduce in order to satisfy the QGSJet-II-2 (p,Fe) range prediction over the entire energy range accessible to KASCADE-Grande (see Fig. 10). Using the modified experimental $S(500)$ values the differences in the energy determination vanishes at lower energies (Fig. 12) (and also the resulting spectrum is comparable to the published one within the range of the systematics uncertainties, see Appendix C).

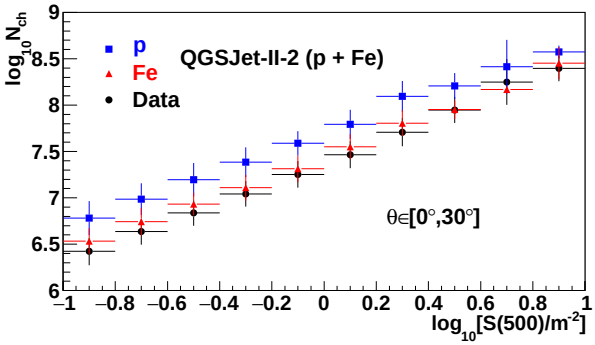

Figure 10: The correlation between the NKG-derived shower size N_{ch} in the standard approach and the $S(500)$ for p and Fe simulated events and for experimental data.

We therefore conclude that the systematic shift between the two KASCADE-Grande results is mainly due to the simulations that do not accurately describe the shape of the lateral density distributions as they appear too steep at large radial ranges in comparison to the data. Since the $S(500)$-based method samples most of its information from a reduced radial range at 500 m from the shower axis, it is likely that this method is more sensitive to inaccuracies in the shape of the simulated lateral distribution than the standard approach which samples data from the entire radial range of the lateral density distribution. This is equivalent to saying that a significant (according to Fig. 10 approximately 30% less density) disagreement in shape at 500 m from the shower axis may have significantly less influence on the integrated value N_{ch}. This picture seems to change at higher energies, where $S(500)$ is already in the steeper part of the lateral distribution. But as statistics is low, it cannot be decided if 500 m distance is still the appropriate value for an unbiased energy determination.

We discuss in the following two physics possibilities to explain a different lateral shape of charged particles in EAS by simulations and data:

- A shallower lateral density distribution as desired at large radial ranges is consistent with older showers starting higher in the atmosphere which trans-

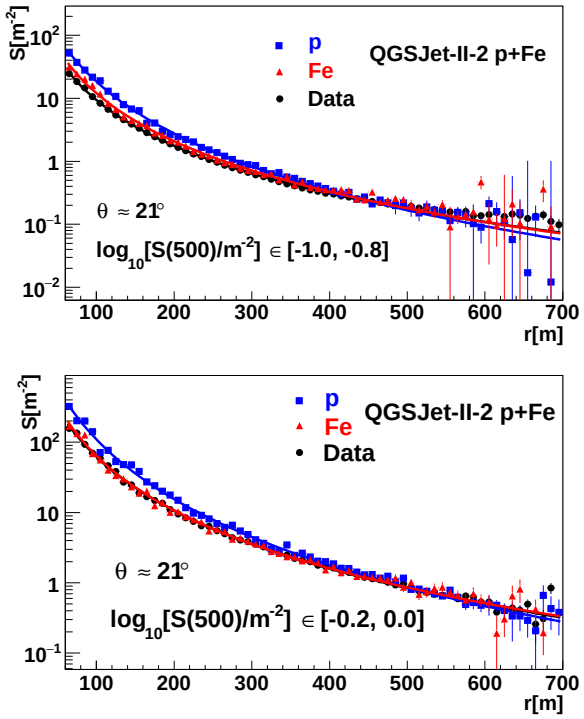

Figure 11: Averaged lateral charged particle density distributions for simulations (CORSIKA/QGSJet-II-2 p and Fe showers) and experimental data, for events with $\log_{10}[S(500)/\mathrm{m}^{-2}]\in$[-1, -0.8](*above*) and $\log_{10}[S(500)/\mathrm{m}^{-2}]\in$[-0.2, 0.0](*below*); we show only events inclined at ≈21° to avoid effects induced by attenuation in the atmosphere; the continuous lines are of a Linsley-type function.

lates into larger cross section for the primary. This solution however seems to contradict the latest results at LHC[5] [28, 29] that do not encourage further increase of the cross sections in most models. Therefore an even larger cross section for the primary does not seem to be the solution for improving the agreement between data and simulations.

- In a second approach to the matter it seems likely that increasing the muon content at large radial ranges in the simulated showers could increase the curvature of the lateral distribution, given that in the lateral distribution the ratio N_μ/N_{ch} is not constant over the entire radial range. At large radial ranges the electron component is practically extinct and the charge component at such ranges is dominated by muons. Two possible mechanism to increase the muon content at large radial ranges

[5] the particle energy of 7 TeV at the LHC translates into a primary energy of approximately 3×10^{16} eV of a proton impinging the atmosphere

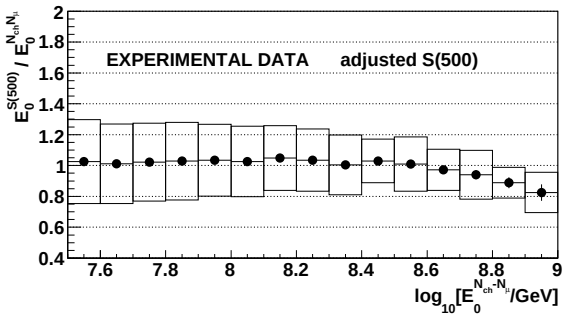

Figure 12: Ratio between the reconstructed energy from $S(500)$, $E_0^{S(500)}$ and $E_0^{N_{ch},N_\mu}$, where the recorded $S(500)$ is corrected to be in agreement with the QGSJet-II-2 Fe prediction. The box errors show the spread of data and the bar errors the error of the mean.

are the increase of muon multiplicity (resulting in an overall increased number of muons), or the increase of muon lateral spread (which produces a flattening in the lateral distribution without affecting the muon size). The two mechanisms are not mutually exclusive and could be combined to some extent. Several other independent investigations show that indeed the measured muon component seem to be richer than the one predicted by simulations (e.g. [30, 31]). A preliminary test of this hypothesis using a set of CORSIKA simulations based on the EPOS 1.99 hadronic interaction model has been performed. One of the differences between EPOS 1.99 and QGSJet-II-2 for a given primary is that on average the EPOS simulated showers will contain more muons (a feature which of course would affect both reconstruction methods at KASCADE-Grande). Fig. 13a shows the averaged lateral density distributions like in Fig. 11, but for simulations based on the EPOS 1.99 model. In addition, Fig. 13b,c show similar plots for the case of QGSJet-II-4 and EPOS-LHC hadronic interaction models. With EPOS 1.99 there seems to be better agreement between data and simulations although experimental data are still not inside the (p, Fe) expected range and the shape is still flatter than for the simulated ones. When deriving the primary energy from $S(500)$ with a calibration based on EPOS 1.99 simulations there is indeed a 10% systematic decrease of the primary energy when compared to the case of the QGSJet-II-2 calibration. The observed discrepancy between data and simulations is thus reduced (Fig. 14a), but does not vanish completely indicating that simply increasing the muon multiplicity is not a straightforward solu-

tion to the matter. The tests with simulated showers based on QGSJet-II-4 and EPOS-LHC show that these newer models also do not bring significant changes when compared to their earlier versions (Fig. 13b,c and Fig. 14b,c) in this particular observable. A slight improvement in the post-LHC models compared to earlier versions however could be identified.

In the $S(500)$-based method the simulation-derived calibration is very sensitive to the shape of the simulated lateral distribution and even small deviations in the shape of the distributions can have significant effects in the resulting energy spectrum. The same is true when talking about the fluctuations of the $S(500)$ observable itself. The detected charge particle density at 500 m distance from the shower core can be accompanied by significant fluctuations due to the small number of particles per station or to the fact that in some cases there is no data close to 500 m due to the array size. However, the sensitivity of this method to the shape of the lateral distribution can be turned into a positive feature in evaluating the simulation quality. In contrast to the $S(500)$-based approach, the method based on the N_{ch}-N_{μ} correlation infers the primary energy from the whole range of the lateral distribution and is less affected by small deviations in the shape, local fluctuations or the lack of information in the lateral distribution. In this respect, the reconstruction of the primary energy from the charged particle and muon numbers (shower sizes) is more robust.

5. Conclusions

The primary energy spectrum of cosmic rays in the range of 10^{16} - 10^{18} eV accessible by the KASCADE-Grande experiment has been determined based on a correlation between the total number of charged particles and the muon number. In this paper we presented an approach to reconstruct the primary energy of individual measured air-showers based on another energy estimator, the charged particle density at 500 m distance from the shower axis similarly to that used in experiments like Auger ($S(1000)$ [32]), or AGASA ($S(600)$ [10])[6]. According to the QGSJet-II-2 predictions the $S(500)$-derived energy is composition independent as the density of charged particles at 500 m distance to the shower axis is mass-insensitive for the special case of KASCADE-Grande. A study on simulated events preceded the study on experimental data in order to evaluate the reconstruction efficiency and quality and to derive a calibration curve E_0 - $S(500)$. The analysis has been applied identically to simulated and experimental events.

The $S(500)$-derived primary energy shows a systematic shift when compared to the result of the standard reconstruction approach, but only in case of measured data. In case of simulation both methods result in an energy determination of similar good quality. We attribute the origin of this shift to a disagreement between

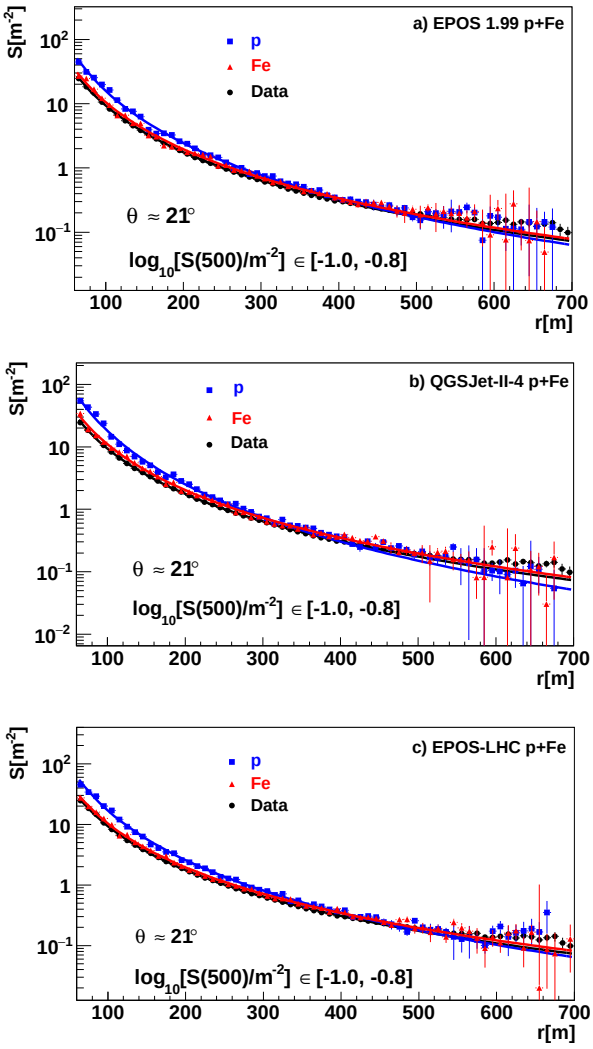

Figure 13: Averaged lateral charged particle density distributions similar to the ones in Fig. 11, but here the simulations are using the EPOS 1.99 (a), QGSJet-II-4 (b) and EPOS-LHC (c) models.

[6]It should be noted that in case of the Auger Observatory the calibration of the value is based on calorimetric measurements by the fluorescence telescopes, whereas in case of AGASA or KASCADE-Grande simulations have to be used.

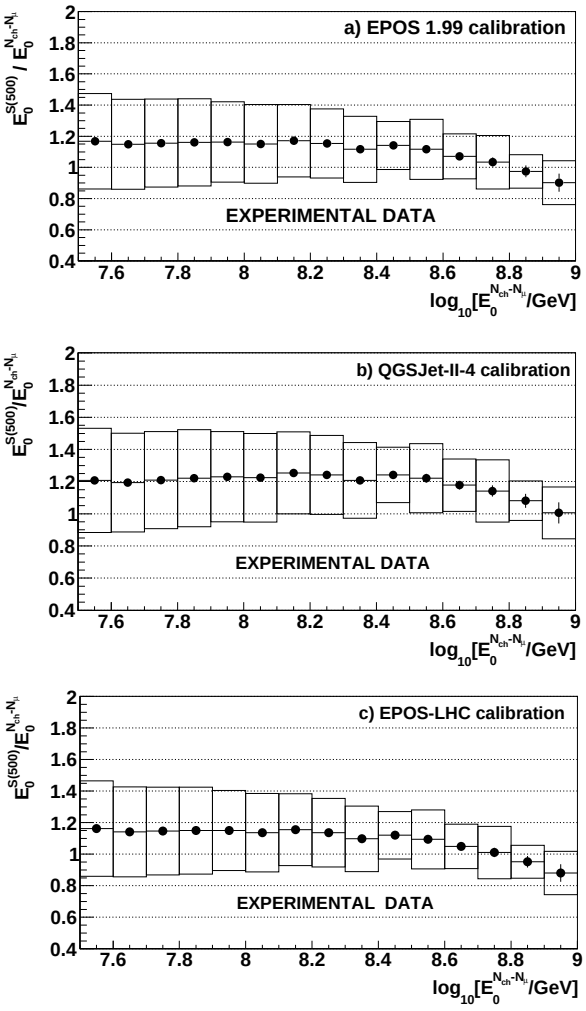

Figure 14: These plots are similar to the one in Fig. 9 but here the $S(500)$-derived energy for KASCADE-Grande is inferred using calibrations based on simulations with EPOS 1.99 (a), QGSJet-II-4 (b) and EPOS-LHC (c).

the shape of simulated lateral distributions and the observed distributions. The simulated lateral distributions are too steep at large radial ranges in comparison with the data. The effect seems to be much weaker at higher energies. This might be due to the fact that KASCADE-Grande measures the particle densities up to 700 m core distance only, while for higher energies muons dominate the lateral distributions at larger distances only. The inconsistency between simulations and data is large enough to justify most of the shift between the energy spectra from the two methods. Methodical or detector effects are excluded to be a major effect as several tests were performed like using different lateral distribution functions, independent analysis codes, or the analysis of subsamples of the total shower sample.

We have discussed two possible solutions to improve the agreement between data and simulations. While one solution (higher cross sections) might be disfavored by recent results at the LHC, the possible solution of predicting a higher muon multiplicity possibly combined with spatially adjusted (i.e. flatter) muon lateral distributions seems to be more promising as are the results from preliminary tests based on the EPOS 1.99 or the newer post-LHC interaction models.

When compared to their earlier versions, the QGSJet-II-4 and EPOS-LHC hadronic interaction models do not significantly affect or improve the reconstruction of primary energy from the S(500) observable.

Acknowledgement

The authors would like to thank the members of the engineering and technical staff of the KASCADE-Grande collaboration, who contributed to the success of the experiment. The KASCADE-Grande experiment is supported in Germany by the BMBF and by the 'Helmholtz Alliance for Astroparticle Physics - HAP' funded by the Initiative and Networking Fund of the Helmholtz Association, by the MIUR and INAF of Italy, the Polish Ministry of Science and Higher Education, and the Romanian National Authority for Scientific Research, ANCS-UEFISCDI, project numbers PN-II-ID-PCE-2011-3-0691 and PN-II-RUPD-2011-3-0145. G. Toma acknowledges KIT Karlsruhe for supporting and hosting part of this research activity and also DAAD for supporting part of the study in the frame of the doctoral scholarship A/06/09016 Ref. 322.

[1] V. Berezinsky, A. Gazizov, S. Grigorieva, Phys. Rev D74 (4) (2006) 043005
[2] A.M. Hillas, J. Phys. G: Nucl. Part. Phys. 31 (2005) R95
[3] The Pierre Auger and Telescope Array Collaborations, Astrophys. Journ. 794 (2014) 172
[4] W.D. Apel et al., NIM A 620 (2010) 202-215
[5] T. Antoni et al. - KASCADE Collaboration, Nucl.Instr. and Meth. A 513 (2003) 429
[6] M. Aglietta et al. - EAS-TOP Collaboration, Nucl.Instr. and Meth. A 336 (1993) 310
[7] W.D. Apel et al. (KASCADE-Grande collaboration), Astropart. Phys. 36 (2012) 183-194
[8] W.-D. Apel et al. (KASCADE-Grande Collaboration), Physical Review Letters 107 (2011) 171104
[9] W.-D. Apel et al. (KASCADE-Grande Collaboration), Physical Review D 87, 081101(R) (2013)
[10] H.Y. Dai et al., J. Phys. G Nucl. Phys. 14 (1988) 793
[11] A.M. Hillas et al., Proc.12th ICRC, Hobart 3 (1971) 1001
[12] H. Rebel and O. Sima et al. KASCADE-Grande collaboration, Proc. 29th ICRC Pune India 6 (2005) 297; I.M. Brancus et al. KASCADE-Grande collaboration, Proc. 29th ICRC Pune India 6 (2005) 361

[13] D. Heck et al., Report Forschungszentrum Karlsruhe 6019 (1998)
[14] N.N. Kalmykov, S.S. Ostapchenko and A.I. Pavlov, Nucl. Phys. B (Proc. Suppl.) 52B (1997) 17-28; S.S. Ostapchenko, Nucl. Phys. B-Proc. 151 (2006) 143-147; S.S. Ostapchenko, Phys. Rev. D 74 (2006) 014026
[15] T.T. Böhlen, F. Cerutti, M.P.W. Chin, A. Fassò, A. Ferrari, P.G. Ortega, A. Mairani, P.R. Sala, G. Smirnov and V. Vlachoudis, "The FLUKA Code: Developments and Challenges for High Energy and Medical Applications", Nuclear Data Sheets 120, 211-214 (2014)
[16] A. Ferrari, P.R. Sala, A. Fassò, and J. Ranft, "FLUKA: a multi-particle transport code", CERN-2005-10 (2005), INFN/TC_05/11, SLAC-R-773
[17] A. Gherghel-Lascu et al. - KASCADE-Grande collaboration, "Effects of the new hadronic interaction models on the reconstruction of KASCADE-Grande observables", Proc. 34th ICRC 2015, The Hague, Netherlands
[18] K. Werner, F. M. Liu and T. Pierog, Phys. Rev. C 74 (2006) 044902
[19] S. Ostapchenko, Phys. Rev. D83 (2011) 014018
[20] T. Pierog, Iu. Karpenko, J.M. Katzy, E. Yatsenko, K. Werner, arXiv:1306.0121 [hep-ph]
[21] O. Sima et al., Report Forschungszentrum Karlsruhe 6985 (2004)
[22] F. Cossavella et al. - KASCADE-Grande Collaboration, Proc. 30th ICRC 2007, Merida, vol. 4, p. 211; R. Glasstetter et al. - KASCADE-Grande collaboration, Proc. 29th ICRC 2005, Pune, vol. 6, p. 293
[23] G. Toma et al., Proc. 26th ECRS Lisbon Portugal so-134 (2006); GEANT users guide (1997)
[24] O. Sima et al. - KASCADE-Grande collaboration, NIM A 638 (2011) 147-156
[25] J. Linsley et al., Journ. Phys. Soc. Japan 17 (1962) A-III
[26] T. Antoni et al.: Astrop. Phys. 24 (2005) 1
[27] W.-D. Apel et al. - KASCADE Collaboration, Astrop. Phys. 24 (2006) 467
[28] R. Ulrich et al. (Pierre Auger Collaboration), Phys. Rev. Lett. 109, 062002 (2012)
[29] G. Antchev et al. (TOTEM Collaboration), Phys.Rev.Lett. 111 (2013) 1, 012001; Europhys.Lett. 101 (2013) 21004
[30] J.C. Arteaga Velázquez et al. - KASCADE-Grande collaboration, "Tests of HE hadronic interaction models with the muon attenuation length in KASCADE-Grande", Proc. 34th ICRC 2015, The Hague, Netherlands
[31] A. Aab et al. - Pierre Auger Collaboration, Phys. Rev. D 91 (2015) 059901
[32] M. Roth et al. - Pierre Auger Collaboration, Proc. 30th ICRC 2007, Merida, vol. 4, p. 327
[33] M. Nagano et al., J.Phys G Nucl.Phys. 10 (1984) 1295
[34] R. Gold, Argonne National Laboratory Report ANL-6984, Argonne, 1964; H. Ulrich, et al., KASCADE Collaboration, Proc. 27th ICRC, Hamburg, 2001.
[35] G.D. Agostini, DESY94-099 (1994); G.D. Agostini, NIM A 362, 1995, p. 487
[36] J. Friedman, Cern School of computing, Norway, 22, 1974
[37] O. Sima et al., "The reconstruction of the lateral charge particle distributions and the studies of different LDF parameterisations", FZKA Interner Bericht KASCADE-Grande 2005-01, Forschungszentrum Karlsruhe 2005

Appendix A. The Constant Intensity Cut method

Some EAS observables at the detector level are greatly influenced by the zenith angle of the shower because, on average, the particles travel along paths with different lengths in the atmosphere depending on the zenith angle. Such is the case of the $S(500)$ which on average can have different values for the same primaries (E_0, A_0) arriving from different zenith angles. One has to correct for this effect before performing an analysis simultaneously on all recorded EAS events. This is achieved by applying the Constant Intensity Cut (CIC) method [33]. The method is based on the assumption that for a given minimum primary energy above the full efficiency threshold we should record the same flux of primaries (i.e. air showers) from all zenith angles. That is analogous to say that in the integral spectra from different zenith angles equal intensity corresponds to the same primary energy.

We perform several constant intensity cuts on the integral $S(500)$ spectra corresponding to different zenith angles (Fig. A.15) and for each cut we establish a correlation between the $S(500)$ and the corresponding zenith angle (Fig. A.16). To build the integral $S(500)$ spectra we pick the zenith angular intervals in the range [0°,30°] so that they subtend equal solid angles. We fit all values in Fig. A.16 simultaneously with a functional form derived from a second degree polynomial and use this functional form as a correction function to account for the attenuation of $S(500)$. All reconstructed $S(500)$ values are corrected by bringing them to the value they would have at a chosen reference angle. For the present study the reference angle is considered to be 21°, since the zenith angular distribution for the recorded EAS sample peaks at this value. The uncertainty associated to each attenuation-corrected S(500) value is derived from the uncertainties in Fig. A.15 by propagating them through the entire calculus of the CIC method (the uncertainty introduced by the global fit in Fig. A.16 is also taken into account). The CIC correction is thus derived entirely from recorded experimental data and is independent from simulations.

The attenuation length $\Lambda_{S(500)}$ of $S(500)$ is evaluated using a global fit of the attenuation curves assuming exponential attenuation (eq. A.1). The resulting value is $\Lambda_{S(500)} = 402 \pm 7$ g·cm^{-2}.

$$S(500)_\theta = S(500)_{0^\circ} \exp\left[\frac{-X_{0^\circ}}{\Lambda_{S(500)}}(\sec\theta - 1)\right] \quad (A.1)$$

with X_{0° - the atmospheric depth in g/cm^2.

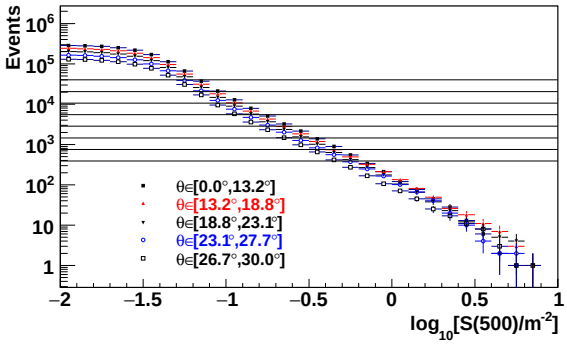

Figure A.15: Integral $S(500)$ spectra; the horizontal lines are constant intensity cuts at arbitrarily chosen intensities.

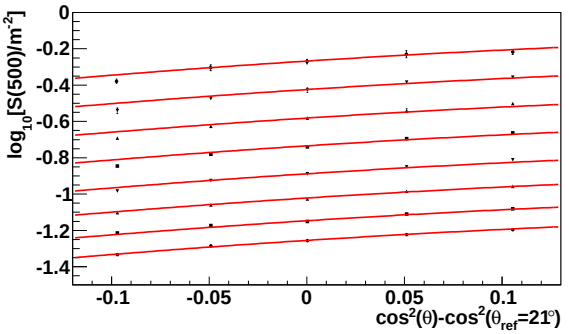

Figure A.16: Variation of the $S(500)$ observable with the angle of incidence; each set of points corresponds to a constant intensity cut in Fig. A.15; the continuous lines show a global fit of all points.

Appendix B. Unfolding based on a response matrix

If a given variable is characterized by intrinsic statistical fluctuations, when representing its spectrum as a histogram with given bin size, the fluctuations will cause the total value stored in each bin to deviate from the true (unknown) value due to events *leaking* to and from neighboring bins. In effect, the reconstructed spectrum is obtained from the true spectrum of the given variable by folding in each bin the contributions from fluctuations in all neighboring bins. This migration depends on the bin size and on the amount of fluctuations and its effects can vary greatly depending on the spectral shape. This is the case of the reconstructed energy spectrum which is very steeply decreasing. Given the steep decrease of the spectrum, it is expected that contributions into neighboring bins will have a greater effect towards higher energies where the flux is much lower. This affects the flux value and simultaneously the spectral index and a correction should be applied in order to compensate. Such a correction is derived using simulated showers and is based on a response matrix in which we plot the probabilities $P(E_j^{rec}, E_i^{true})$ that an energy E_i^{true} is reconstructed as energy E_j^{rec} (where $E_i^{true}/eV \in [10^{16}, 10^{19.5}]$ thus covering the energy range of interest where such effects are of importance). To unfold the effects of fluctuations and infer the true energy spectrum one has then to solve a system of equations as eq. B.1.

$$N^{rec}(j) = \sum_{i=1}^{N_{bins}} P(E_j^{rec}, E_i^{true}) N^{true}(i) \qquad \text{(B.1)}$$

where $\sum_{j=1}^{N_{bins}} P(E_j^{rec}, E_i^{true}) = 1$.

The system is solved iteratively by applying a method based on the Gold algorithm [34] and then the result is compared with the result of another approach based on the Bayes algorithm [35] (applied also iteratively). For a sufficiently large number of iterations the results of the two methods converge (Fig. B.17). For each unfolding procedure, a smoothing was applied to the result of each intermediate iteration in order to avoid fluctuations amplifying from each iteration to the next. This smoothing was based on the 353HQ-twice algorithm [36]. Additionally, the simulation-derived response matrix has been smoothed in order to reduce the effects induced by the statistical fluctuations in the Monte Carlo sample. To smooth the response matrix, the information in each bin of true energy is fitted with a Gauss-Landau convolution and the parameters of the convolution function are then parametrized with the true energy.

The unfolding procedures based on the Gold and Bayes algorithms were tested by comparing the measured spectra with the forward folded ones and good agreement was observed.

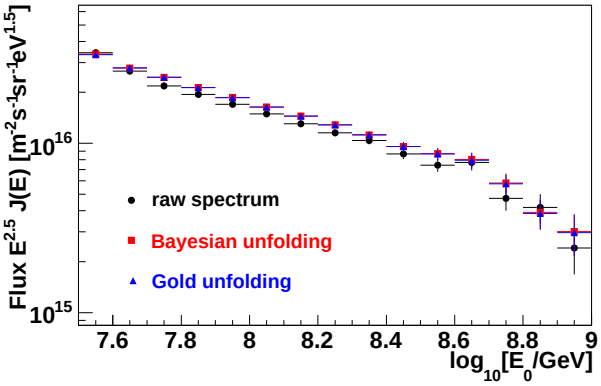

Figure B.17: Results of the Bayes and Gold unfolding algorithms.

Appendix C. The energy spectrum based on $S(500)$ and its systematic uncertainties

The experimental energy spectrum as inferred from the presented approach is shown as $E_0^{S(500)}$ in Fig. C.18 along with the result of KASCADE [26] towards lower energies and with the result from the standard approach [7] as $E_0^{N_{ch}-N_\mu}$. It is important to note that the KASCADE spectrum is inferred from a procedure using the QGSJet-01 model for high energy interactions, with different specific systematics than the QGSJet-II-2 used to infer the two KASCADE-Grande spectra. The figure shows also the resulting spectrum obtained when using EPOS 1.99 as basis for the calibration.

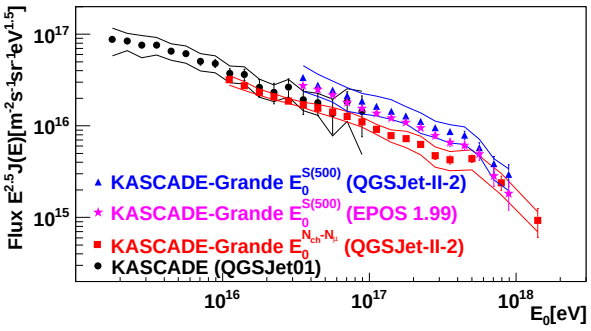

Figure C.18: Primary energy spectra for KASCADE [26] and KASCADE-Grande [7]; the bands with continuous lines show the estimated systematic uncertainty. In this plot the $S(500)$-derived energy spectra for KASCADE-Grande are inferred using calibrations based on simulations with QGSJet-II-2 and EPOS 1.99.

The reconstruction of energy from S(500) relies on a considerable number of parameters that can vary substantially on an arbitrary basis. By propagating through the calculus these variations can lead to fluctuations of the obtained flux. We identify such free parameters and allow them to change within reasonable limits. The resulting variation of energy flux in % is evaluated in each case.

- The accuracy of the S(500) reconstruction
  The S(500) energy estimator is derived from a fit according to [25]. The quality of this fit is significantly affected by the number of stations and also by their position inside the lateral density distribution. The fluctuations in the reconstructed S(500) act as a source of uncertainty and amount to $\approx$ 16.5% at $E_0 = 10^{17}$ eV, decreasing with energy to $\approx$ 8% at $E_0 = 10^{18}$ eV [37].

- Uncertainties in the $E_0 - S(500)$ calibration
  The simulation-derived calibration curve is obtained by a fit procedure and each parameter is characterized by an uncertainty. In order to evaluate the effects of these uncertainties in terms of systematics of the energy flux, the fit parameters are allowed to change according to their uncertainty and the primary energy spectrum is reconstructed in this particular new case. The contribution of this source amounts for a systematic uncertainty of $\approx$ 1% at $E_0 = 10^{17}$ eV, increasing with energy to $\approx$ 6% at $E_0 = 10^{18}$ eV.

- The spectral index of the simulated event sample
  The simulated shower sample that was used throughout this study was weighted on an event by event basis to emulate a primary energy spectrum with a spectral index $\gamma = -3$, close to the natural index of the cosmic ray spectrum, but not exactly the same. The reconstruction is repeated for the cases $\gamma = -2.8$ and $\gamma = -3.2$ and the difference between the fluxes obtained in these two cases is considered as systematic uncertainty. This source amounts for $\approx$ 2% at $E_0 = 10^{17}$ eV, increasing slightly with energy to $\approx$ 4% at $E_0 = 10^{18}$ eV.

- Influence of the Monte-Carlo statistics on the fit parameters
  The simulated shower sample used for energy calibration is generated by a Monte Carlo algorithm which introduces fluctuations differently for different energy ranges, since the energy spectrum is a power law and at high energies there are much less events available for analysis than at lower energies. In order to estimate the effect of these fluctuations, the energy range is divided into 3 sub-ranges and the energy calibration is performed for every sub-range. The new parameterizations will vary slightly from one case to the other due to Monte Carlo fluctuations. The reconstruction is being performed for each particular parametrization and the results are compared. For every energy bin, the difference between the maximum reconstructed flux and the minimum value defines the systematic uncertainty from this source. It amounts for $\approx$ 2% at $E_0 = 10^{17}$ eV, increasing with energy to $\approx$ 8% at $E_0 = 10^{18}$ eV.

- The systematic error introduced by the CIC
  The CIC (Appendix A) method provides an attenuation-corrected $S(500)$ with an associated uncertainty resulting from the CIC method itself. This acts as another source of systematic uncertainty, as the corrected $S(500)$ is converted to energy. To evaluate the contribution of the CIC

method to the overall systematics we allow the corrected $S(500)$ value of each event to change according to the CIC-specific uncertainty. The contribution to the resulting energy flux is rather small, below 1% over the entire energy range.

- Choosing a specific reference angle for which to perform the $S(500)$ correction of attenuation
  When correcting the $S(500)$ for attenuation, a certain reference angle is chosen. Since the experimental zenith angular distribution is peaked at 21°, the reference angle was chosen to be 21° in order to have the CIC method significantly affecting as few showers as possible. However it is possible to choose another angle as well without changing the relevance of the final result, but the correction would affect each shower differently depending on our choice for a reference angle. We are choosing as reference angles the extreme cases 0° and 30° and we compare the resulting spectra after applying CIC for these reference angles. The difference between these spectra defines the contribution of this uncertainty source and it is $\approx 6\%$ at $E_0 = 10^{17}$ eV increasing to $\approx 14\%$ at $E_0 = 10^{18}$ eV.

- The response matrix correction
  The response matrix correction (see Appendix B) involves complex mathematical operations which contribute to the final systematic uncertainties. To evaluate this contribution test spectra have been generated by introducing random Poissonian noise in the raw un-corrected energy spectrum and then by unfolding it. The test spectra are forward folded (the inverse operation of the unfolding procedure) and then re-unfolded. The average difference between the re-unfolded spectra and the average of the test spectra is used to define the contribution of the response matrix correction. It contributes with about 4% over the entire energy range.

- Hadronic interaction model
  The combination of QGSJet-II-2 and FLUKA models has been used for all studies on simulated events and it is expected that the model itself introduces a systematic effect when describing certain shower properties. To obtain a rough estimate of this systematic a second calibration has been derived from simulations based on the EPOS 1.99 model and on average the energy variation with the new calibration is systematically $\approx 10\%$ lower than for QGSJet-II-2. Similarly, when we treat the EPOS shower sample as experimental data and reconstruct it using the calibration based on the QGSJet-II-2 model we obtain a systematic $\approx 10\%$ overestimation of the energy. This contribution is only evaluated here, but not included in the systematic uncertainty band in Fig. C.18, Section 4.1.

The above method-specific sources (therefore excluding the hadronic interaction models) introduce a combined systematic uncertainty of $\approx 32\%$ in the energy flux at $E_0 = 10^{17}$ eV increasing up to $\approx 45\%$ at $E_0 = 10^{18}$ eV.